One of the possible mechanisms for ion-induced closing of the nanochannels is the swelling of the AAO film caused by gallium implantation. Such radiation-induced swelling of material is well-documented; however, it is unlikely to be the key factor because the nanochannels have pore radii of ≈ 20 nm and wall thicknesses of ≈ 30 nm, and the swelling factor needed for completely closing the nanochannels would be as large as ≈ 67 %. In comparison with the ≈ 2% swelling of silicon caused by 50 keV gallium-ion bombardment,[20] such a hypothetical swelling factor of alumina appears unrealistic. More likely, some other mechanisms are responsible for the ion-induced closing. For example, redeposition of sputtered material onto the sidewalls of the pore openings could be among the contributors to the initial phase of the channel closing. Since the longitudinal range and longitudinal straggling of 50 keV gallium in alumina is calculated to be as large as 46 nm and 15 nm respectively,[21] material could be sputtered from the sidewall (≈ 30 nm) of a nanochannel even after it is covered by the capping layer (≈ 20 nm). Therefore, the material ejected from the buried sidewall could be redeposited onto the bottom of the capping layer, replenishing the material sputtered from its top surface. Another possible mechanism is the ion-induced lateral migration and/or diffusion of material, which could also, in principle, build up the initial capping layer and maintain its equilibrium thickness afterwards. Apparently, more detailed studies are needed to help clarify the mechanisms responsible for this fascinating phenomenon of ion-induced closing of nanochannels on an AAO film.

In conclusion, we have employed FIB to selectively close nanochannels of an ordered array on an AAO film, thereby fabricating special templates with nanochannels arranged in certain custom-designed geometries. The closing of the nanochannels can be monitored in situ by FIB imaging during the closing process. The capability to fabricate square, linear, and annular arrays is demonstrated, and is extended to the extreme case where an isolated individual nanochannel is closed. This technique for creating a custom-designed array of nanochannels with a high aspect ratio can be used to fabricate specially designed filters and templates, upon which various nanocomposites and nanodevices could be built. The mechanism for the ion-induced closing of nanochannels on AAO remains to be understood.

Experimental

High-purity annealed aluminum samples were prepared by electropolishing in a mixed solution of 50 % $HClO_4$ and C_2H_5OH (1:5 v/v) at 5 °C under constant stirring until the root-mean-square roughness of a 10 μm × 10 μm surface area was ≈ 1 nm, as measured by contact-mode atomic force microscopy. A 50 keV gallium focused ion beam with a diameter of ≈ 10 nm and beam current of 1.1 pA was employed to create arrays of hexagonal close-packed single-pixel concave pits on polished, polycrystalline-aluminum surfaces. The dwell time was 9 ms pixel^{-1}, and the lattice constant of the array was set to 100 nm in order to match the anodization electrolyte and voltage used in the experiments. The anodization was carried out in 0.3 M oxalic acid solution at 3 °C with a constant voltage of 40 V. After anodization, the nanochannels were opened in a 5 wt.-% solution of phosphoric acid (H_3PO_4) at room temperature. To create a freestanding anodic aluminum oxide film, the remaining aluminum substrate was removed by a saturated $HgCl_2$ solution. If needed, the barrier layer, i.e., an oxide layer on the bottom of the nanochannels, was etched by a 5 wt.-% H_3PO_4 solution, also at room temperature, for 40 min.

Received: March 12, 2004
Final version: July 26, 2004

[1] Y. Li, G. W. Meng, L. D. Zhang, F. Phillipp, *Appl. Phys. Lett.* **2000**, *76*, 2011.
[2] T. G. Tsai, K. J. Chao, X. J. Guo, S. L. Sung, C. N. Wu, Y. L. Wang, H. C. Shih, *Adv. Mater.* **1997**, *9*, 1154.
[3] J. S. Suh, J. S. Lee, *Appl. Phys. Lett.* **1999**, *75*, 2047.
[4] H. Masuda, M. Satoh, *Jpn. J. Appl. Phys., Part 2* **1996**, *35*, L126.
[5] M. Nakao, S. Oku, T. Tamamura, Y. Yasui, H. Masuda, *Jpn. J. Appl. Phys., Part 1* **1999**, *38*, 1052.
[6] H. Masuda, K. Fukuda, *Science* **1995**, *268*, 1466.
[7] J. Li, C. Papadopoulos, J. Xu, *Nature* **1999**, *402*, 253.
[8] H. Masuda, F. Hasegwa, S. Ono, *J. Electrochem. Soc.* **1997**, *144*, L127.
[9] A. P. Li, F. Müller, A. Birner, K. Nielsch, U. Gösele, *J. Appl. Phys.* **1998**, *84*, 6023.
[10] H. Masuda, H. Yamada, M. Satoh, H. Asoh, *Appl. Phys. Lett.* **1997**, *71*, 2770.
[11] C. Y. Liu, A. Datta, Y. L. Wang, *Appl. Phys. Lett.* **2001**, *78*, 120.
[12] N. W. Liu, A. Datta, C. Y. Liu, Y. L. Wang, *Appl. Phys. Lett.* **2003**, *82*, 1281.
[13] J. Li, D. Stein, C. McMullan, D. Branton, M. J. Aziz, J. A. Golovchenko, *Nature* **2001**, *412*, 166.
[14] C. Zhou, M. R. Despande, M. A. Reed, *Appl. Phys. Lett.* **1997**, *71*, 611.
[15] D. C. Ralph, C. T. Black, M. Tinkham, *Phys. Rev. Lett.* **1995**, *74*, 3241.
[16] M. M. Deshmukh, D. C. Ralph, M. Thomas, J. Silcox, *Appl. Phys. Lett.* **1999**, *75*, 1631.
[17] C. Y. Liu, A. Datta, N. W. Liu, C. Y. Peng, Y. L. Wang, *Appl. Phys. Lett.* **2004**, *84*, 2509.
[18] P. H. La Marche, R. Levi-Setti, Y. L. Wang, *J. Vac. Sci. Technol., B: Microelectron. Process. Phenom.* **1983**, *B1*, 1056.
[19] Y. L. Wang, Z. Shao, in *Advances in Electronics and Electron Physics* (Ed: P. W. Hawkes), Vol. 81, Academic, Boston, MA **1991**, p. 177.
[20] J. B. Wang, A. Datta, Y. L. Wang, *Appl. Surf. Sci.* **1998**, *135*, 129.
[21] J. F. Zeigler, J. P. Biersack, SRIM (TRIM 90) Simulation Package (1995), IBM Research, 28-024 Yorktown, NY 10598.

Single-Catalyst Confined Growth of ZnS/Si Composite Nanowires**

By *Jinhua Zhan*,* *Yoshio Bando*, *Junqing Hu*, *Takashi Sekiguchi*, and *Dmitri Golberg*

One-dimensional (1D) nanomaterials have attracted considerable attention due to their potential application as building blocks in nanoscale circuits and optoelectronic devices.[1–3] The

[*] Dr. J. Zhan, Prof. Y. Bando, Dr. J. Hu, Dr. T. Sekiguchi, Dr. D. Golberg
Advanced Materials Laboratory and Nanomaterials Laboratory
National Institute for Materials Science
Namiki 1-1, Tsukuba, Ibaraki 305-0044 (Japan)
E-mail: ZHAN.Jinhua@nims.go.jp

[**] Supporting Information is available online from Wiley InterScience or from the author.

DOI: 10.1002/adma.200400585

ADVANCED MATERIALS

vapor–liquid–solid (VLS) growth process has been extensively used for the synthesis of 1D nanostructures. The key feature during VLS growth is the existence of an alloy droplet that caps one end of a 1D nanostructure. This promotes anisotropic crystal growth.[4,5] In a VLS-growth process, the metal catalysts are rationally selected according to a given phase diagram. A catalyst may act as a preferential site for the absorption of vapors to form a liquid alloy. Once an absorbed reactant is supersaturated within a liquid alloy at a given temperature, it nucleates from a supersaturated-liquid droplet. Further condensation of the reactant vapors results in the axial growth of a 1D structure. Generally, the diameter of the nanowires grown via a VLS process is limited by the diameter of the liquid-alloy droplets. VLS processes have been widely used to produce 1D nanostructures from various inorganic solids including elemental semiconductors (Si, Ge), group III–V semiconductors, and group II–VI semiconductors using Au or Fe nanoparticles as catalysts.[6–8] Development of new functional nanoscale electronic devices requires utilization of novel heterostructures. The block-by-block growth of Si/SiGe and InAs/InP superlattice nanowires along the axial direction using Au-nanoparticle catalysts has been reported.[9–11] Based on their crystallographic similarity, side-by-side 1D TiO_2/SnO_2 and ZnS/Si composite nanostructures have been generated by laser-ablation deposition of TiO_2 over SnO_2 nanobelts and chemical vapor deposition of ZnS on Si nanowires, respectively.[12,13]

Zinc sulfide, a direct wide-bandgap semiconductor (3.68 eV at 300 K), plays an important role in optoelectronic applications.[14] Silicon has long been considered as the optimal material for electronics used in information technologies, and has recently been proposed to be the optimal material for photonics.[15] 1D zinc sulfide and silicon nanostructures have been reported by many groups.[16,17]

The melting point of elemental tin is approximately 232 °C.[18] Tin can form a liquid alloy with silicon and zinc sulfide at high temperatures, but, by contrast, its solubility in solid silicon or zinc sulfide is negligible.[19] Therefore, it is reasonable to assume that elemental tin can be used to simultaneously catalyze the anisotropic growth of zinc sulfide and silicon nanowires. If two substances are evaporated simultaneously, tin nanoparticles may catalyze the growth of composite nanowires. Herein, we demonstrate a typical example of bimorph-composite nanowires via single-catalyst confined growth. ZnS/Si side-by-side 1D heterostructures were generated through this novel tin-catalyzed growth mechanism. The diameters of the 1D composite nanostructures can reach as low as approximately 15 nm.

During the synthesis process, zinc sulfide and silicon powders were thermally co-evaporated at a high temperature (approximately 1100 °C) with a small amount of tin sulfide as an additive. Then, silicon and zinc sulfide vapors condensed on metallic-tin droplets at a low temperature (approximately 600 °C), which resulted in the anisotropic growth of silicon and zinc sulfide simultaneously. The powder X-ray diffraction (XRD) pattern of the product, shown in Figure 1A, suggests the co-existence of silicon and zinc sulfide with zinc-blende

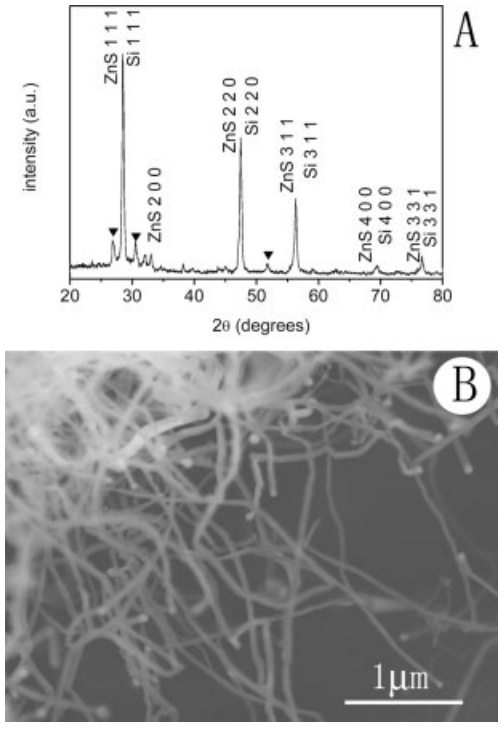

Figure 1. A) XRD pattern of an as-obtained product. Marked peaks (▼) correspond to ZnS with a wurtzite (W) structure. B) Scanning electron microscopy (SEM) image of the composite nanowires.

(ZB) structures. The diffraction peaks marked with filled triangles in Figure 1A could be assigned to wurtzite (W) ZnS. The scanning electron microscopy (SEM) image, shown in Figure 1B, indicates that the product is composed of 1D, high-aspect-ratio nanostructures, and that each nanowire is capped with a spherical catalytic particle.

Detailed structural and chemical analyses of individual composite nanowires were carried out using high-resolution transmission electron microscopy (HRTEM). Figure 2A, a TEM bright-field image of a typical nanowire, clearly shows that the wire is composed of two distinct fragments and capped with a spherical tip. The diameter of the composite nanowire is approximately 90 nm. The tip and the two distinct wire fragments were examined using energy-dispersive X-ray spectroscopy (EDX) with a nanoprobe. The corresponding EDX spectra are shown in Figures 2B–D. It is evident that the spherical cap is made of metallic tin. The part exhibiting a brighter contrast is composed of silicon, whereas that with a darker contrast is composed of zinc sulfide with a composition of 49.4 % Zn and 50.6 % S. High-resolution TEM images of a ZnS domain, a Si domain, and the interface between them are displayed in Figures 3A–C, respectively. As seen in these images, both fragments are structurally uniform. The clearly resolved fringes with a 3.10 Å separation are typical for the {111} *d*-spacing of diamond-like Si and ZB ZnS. The interface between the ZnS and Si fragments is homogeneous and atomically sharp. It has been reported that ZnS thin films can grow epitaxially on a silicon substrate.[20] In fact, the similarity be-

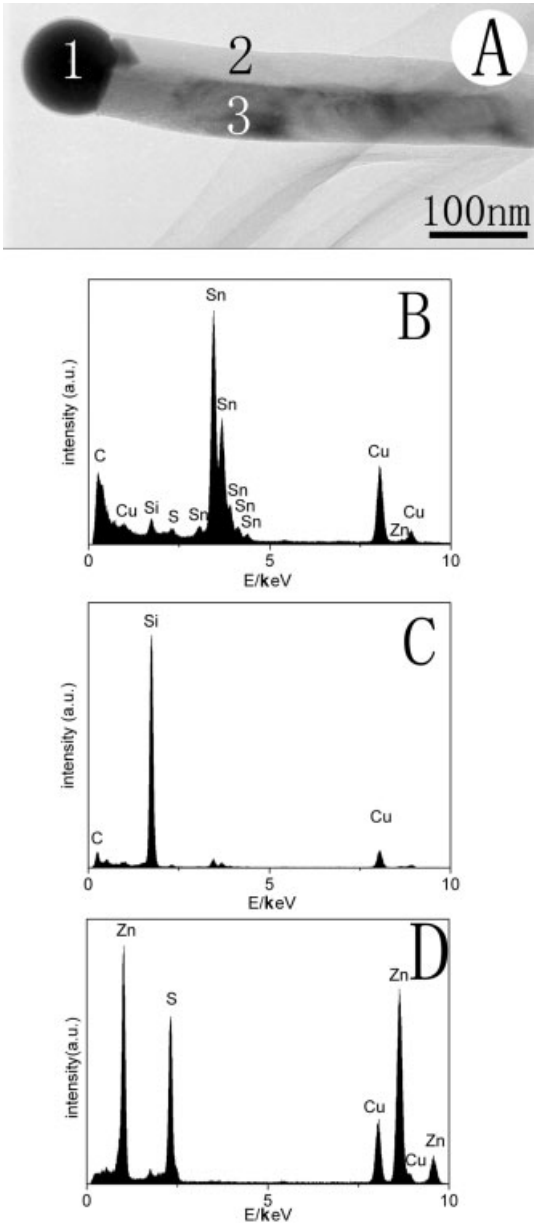

Figure 2. A) TEM image of a typical composite nanowire. B–D) Nanoprobe energy-dispersive X-ray (EDX) spectra of the regions labeled 1 (B), 2 (C), and 3 (D) on the nanowire.

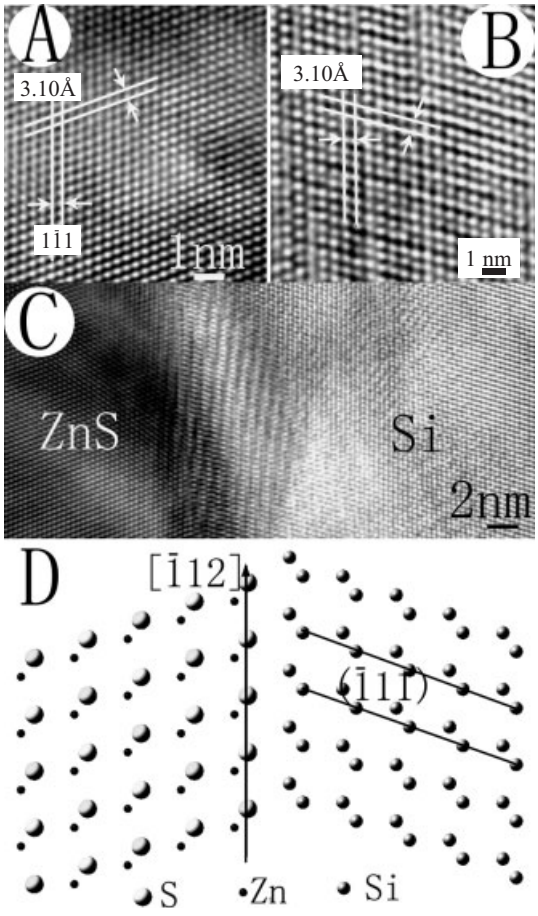

Figure 3. HRTEM images of A) a ZnS-wire fragment; B) a Si-wire fragment; and C) an interface between two fractions. D) Structural model showing the crystallographic relationship between the ZnS and Si fragments.

tween the ZB ZnS and the diamond-like Si lattice constants results in only a marginal lattice mismatch of ~0.5 % (ZB ZnS: $a = 5.4060$ Å, Joint Committee on Powder Diffraction Standards (JCPDS) Card No. 05-0566; diamond-like Si: $a = 5.43088$ Å, JCPDS Card No. 27-1402). It is worth noting that both fragments in the ZnS–Si composite nanowires have a twin-like crystallographic relationship, as displayed in the HRTEM images: $(1\bar{1}1)_{ZnS}$ is parallel to $(1\bar{1}1)_{Si}$, while $(\bar{1}11)_{ZnS}$ and $(\bar{1}11)_{Si}$ are mirror planes of $(1\bar{1}1)_{Si}$. The growth direction of the composite nanowires is close to $[\bar{1}12]_{Si}$. Figure 3D is a structural model of the [110] projection of ZB ZnS and diamond-like Si crystal lattices, which illustrates the structural relationship between the two fragments in Figures 3A–C.

70 % of the nanowires possess diameters of approximately 90 nm, and 30 % of them have diameters of approximately 15 nm. The composite nanowires exhibiting nearly similar diameters frequently aggregated together. The TEM image (Supporting Information, Fig. S1) shows that these nanowires are also capped with spherical particles. Figure 4A, a TEM image of a typical composite nanowire ~18 nm in diameter, also reveals two distinct parts. Nanobeam EDX analyses of the thin composite nanowires indicate side-by-side ZnS/Si regions and spherical, metallic-tin tips, similar to the thick wires discussed above. Further HRTEM studies provided detailed structural information on the ZnS and Si wire fragments. Figure 4B, a HRTEM image of the interface between the ZnS and Si fractions, verifies that ZB ZnS grew epitaxially on diamond-like Si, in contrast to the observed twin-like crystallographic relationship in the thicker composite nanowires. The interface between the ZnS and Si fractions resulting from epitaxial growth is shown schematically for the [110] projection of diamond-like Si and ZB ZnS in Figure 4C. The preferred

ADVANCED MATERIALS

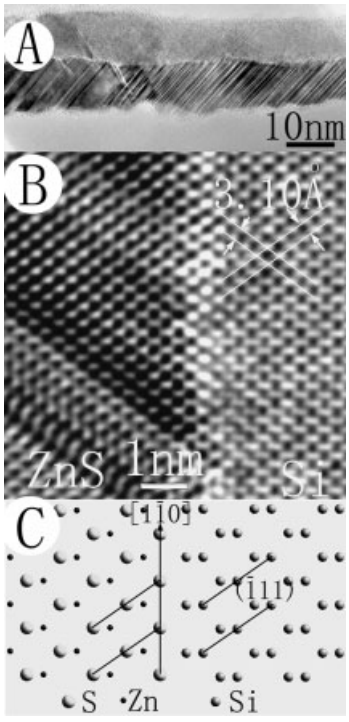

Figure 4. A) TEM image of a single, thin composite nanowire; B) HRTEM image displaying the interfacial structure of the composite nanowire; and C) structural model showing the crystallographic relationship between the ZnS and Si wire fragments in the nanowire.

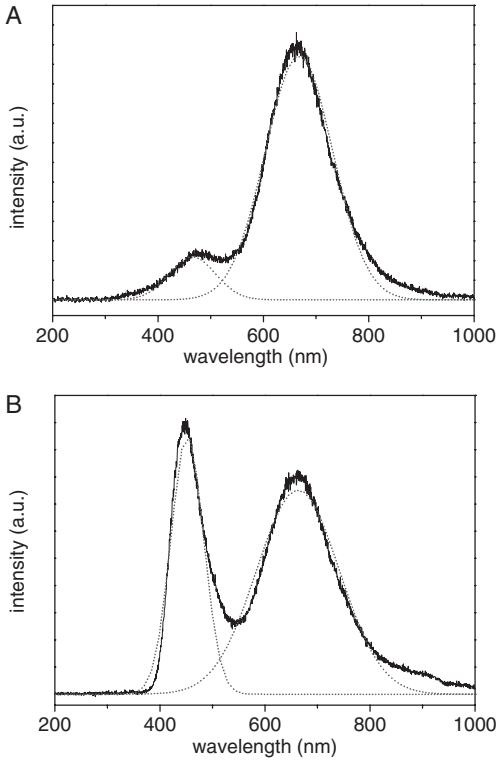

Figure 5. CL spectra recorded at 17 K from composite nanowires with approximate diameters of A) 90 nm; and B) 15 nm. Dotted lines represent peaks after deconvolution.

growth orientation of a thin composite nanowire is close to $[1\bar{1}0]_{Si}$. The Si fragment is structurally homogeneous, whereas the diagonal stripes within the ZnS domain (Fig. 4A) suggest its structural inhomogeneity. HRTEM studies revealed the coexistence of ZB ZnS and wurtzite ZnS (W-ZnS) (Supporting Information, Fig. S2). A region between the two dark lines consists of a hexagonal phase oriented along the [100] direction (Fig. S2). The existence of a W-ZnS phase in thin composite nanowires may account for the presence of the low-intensity diffraction peaks of W-ZnS marked with filled triangles in the XRD pattern (Fig. 1A). In the thin composite nanowires, $(001)_{W\text{-}ZnS}$ is parallel to $(1\bar{1}1)_{ZB\text{-}ZnS}$ and $(1\bar{1}1)_{Si}$. Both ZB-ZnS and W-ZnS phases can be considered as stacked ZnS_4 tetrahedrons. ABCABC-type stacking formed the ZB-ZnS phase, whereas ABAB-type stacking formed the W-ZnS phase. The two structures can be transformed by changing the stacking sequences along the $[111]_{ZB\text{-}ZnS}$ or $[001]_{W\text{-}ZnS}$ directions.

The high-spatial-resolution cathodoluminescence (CL) spectra (Fig. 5) collected from either thick or thin composite nanowires always exhibited two peaks. The emission peak at approximately 685 nm (1.81 eV) may be attributed to the Si fragments within the composite nanowires, which is consistent with data in the literature.[17] The peaks at 465 nm (2.67 eV) in Figure 5A and at 452 nm (2.7 eV) in Figure 5B may be attributed to the ZnS fragments within the nanowires. These peaks originated from the native defects in ZnS, including vacancies and dislocations. The thinner composite nanowires contained much higher defect densities than the thicker ones; therefore, they naturally displayed much more intense blue-light emission.

During the synthetic process, tin sulfide plays an important role in the thermal evaporation of silicon and zinc sulfide to finally generate composite nanowires. The as-obtained composite nanowires were capped with metallic-tin droplets, which is the key feature of the VLS-growth mechanism. The growth process is shown schematically in Fig. 6. Most importantly, in the absence of tin sulfide, the nanowires cannot be

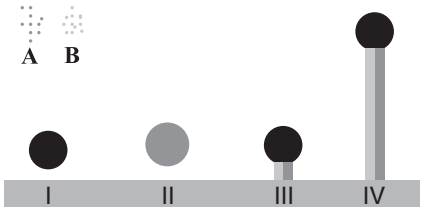

Figure 6. Schematic of growth mechanism for the formation of 1D composite nanostructures. I) Formation of liquid-Sn droplets, where A and B are ZnS and Si vapors, respectively; II) condensation of ZnS and Si vapors on Sn droplets; III) simultaneous crystal nucleation of ZnS and Si; and IV) anisotropic crystal growth of ZnS and Si.

generated. Based on thermodynamics,[21] the involved chemical reactions may proceed as follows:

$$Si + ZnS(s) \rightarrow Zn(g) + SiS(g)$$
$$\Delta G^{\circ}_{1400\ K} = 29.774\ kJ\ mol^{-1},\ \log K_{1400\ K} = -1.110 \quad (1)$$

$$ZnS(s) \rightarrow Zn(g) + 1/2\ S_2(g)$$
$$\Delta G^{\circ}_{1400\ K} = 109.016\ kJ\ mol^{-1},\ \log K_{1400\ K} = -4.067 \quad (2)$$

$$Si(s) \rightarrow Si(g)$$
$$\Delta G^{\circ}_{1400\ K} = 243.306\ kJ\ mol^{-1},\ \log K_{1400\ K} = -9.078 \quad (3)$$

$$Zn(g) + SiS(g) \rightarrow Si(s) + ZnS(s)$$
$$\Delta G^{\circ}_{900\ K} = -138.783\ kJ\ mol^{-1},\ \log K_{900\ K} = 8.055 \quad (4)$$

$$SiS(g) \rightarrow Si(s) + \tfrac{1}{2}\ SiS_2(s)$$
$$\Delta G^{\circ}_{900\ K} = -62.3205\ kJ\ mol^{-1},\ \log K_{900\ K} = 3.617 \quad (5)$$

From a thermodynamic point of view, an equilibrium vapor pressure of $P_{Zn(g)}$ and $P_{SiS(g)}$, created according to Equation 1 at 1400 K, is as high as 28.22 kPa. On the other hand, the self-evaporation of ZnS, Equation 2, is generally preferred, owing to the fact that the reaction between Si and ZnS must overcome a diffusion barrier. The self-evaporation of Si is negligible, for the equilibrium vapor pressure $P_{Si(g)}$, created according to Equation 3 at 1400 K, is as low as 8.47×10^{-8} kPa. SnS melts at 1155 K. Liquid SnS can considerably reduce the diffusion energy for the reaction between solid-state Si and ZnS; thus, Equation 1 becomes preferred. From a kinetic viewpoint, SnS can accelerate the reaction (Eq. 1). At a lower temperature, Zn and SiS vapors are inclined to recombine, producing Si and ZnS (Eq. 4). Although SiS(g) can potentially decompose to produce Si and SiS_2 (Eq. 5), Equation 4 is considerably preferred in the presence of Zn(g). Moreover, the decomposition of SnS results in the formation of tin vapor. The tin vapor condenses at a lower temperature to produce liquid-tin droplets, which then absorb ZnS and Si vapors and catalyze the anisotropic growth of ZnS/Si composite nanowires.

In summary, side-by-side ZnS/Si composite nanowires have been obtained through thermal co-evaporation of ZnS and Si powders with a small amount of tin sulfide as an additive. The composite nanowires are generally capped with metallic-tin particles, in accord with the VLS mechanism. The composite nanowires with smaller diameters (~15 nm) have stronger blue-light emission than those with larger diameters (~90 nm). The generation of composite nanowires has been discussed based on thermodynamic and kinetic points of view. Through a similar approach, Cd_4SiS_6/Si composite nanowires have also been obtained (data not shown). The single-catalyst confined growth of other 1D nanoscale heterostructures in various solids is also envisaged.

Experimental

The composite nanowires were synthesized in a vertical induction furnace consisting of a fused-quartz tube and an induction-heated cylinder made of high-purity graphite, coated with a carbon-fiber thermal-insulating layer. The furnace has an inlet C-pipe and an outlet C-pipe on its top and base, respectively. A graphite crucible, containing 0.97 g ZnS, 0.28 g Si, and 0.01 g SnS, was placed at the center of the cylinder zone. After evacuation of the quartz tube to ~10^{-3} Pa, a pure-N_2 flow was set within the carbon cylinder at a constant rate of 1000 sccm. The furnace was heated further and kept at 1100 °C for 1 h. After the reaction was terminated and the furnace cooled to room temperature, a yellow product was collected from the outlet of the graphite induction-heated cylinder. The product then was characterized using X-ray diffraction (RINT 2200) with Cu Kα radiation, scanning electron microscopy (JSM-6700F), and high-resolution transmission electron microscopy (JEM-3000F, equipped with an energy dispersive X-ray spectroscopy unit). Cathodoluminescence (CL) spectra were collected at 17 K with a high-spatial-resolution CL system performing at 5 kV and 1.2 nA.

Received: April 20, 2004
Final version: August 9, 2004

[1] Y. Cui, C. M. Lieber, *Science* **2001**, *291*, 851.
[2] X. F. Duan, Y. Huang, R. Agarwal, C. M. Lieber, *Nature* **2003**, *421*, 241.
[3] E. Comini, G. Faglia, G. Sberveglieri, Z. W. Pan, Z. L. Wang, *Appl. Phys. Lett.* **2002**, *81*, 1869.
[4] Y. Wu, P. Yang, *J. Am. Chem. Soc.* **2001**, *123*, 3165.
[5] *Whisker Technology* (Ed: A. P. Levitt), Wiley, New York **1970**.
[6] Y. Xia, P. Yang, Y. Sun, Y. Wu, B. Mayers, B. Gates, Y. Yin, F. Kim, Y. Yan, *Adv. Mater.* **2003**, *15*, 353.
[7] X. F. Duan, C. M. Lieber, *Adv. Mater.* **2000**, *12*, 298.
[8] D. Wang, H. Dai, *Angew. Chem. Int. Ed.* **2002**, *41*, 4783.
[9] Y. Wu, R. Fan, P. Yang, *Nano Lett.* **2002**, *2*, 83.
[10] M. S. Gudiksen, L. J. Lauhon, J. Wang, D. C. Smith, C. M. Lieber, *Nature* **2002**, *415*, 617.
[11] M. T. Bjork, B. J. Ohlsson, T. Sass, A. I. Persson, C. Thelander, M. H. Magnusson, K. Deppert, L. R. Wallenberg, L. Samuelson, *Nano Lett.* **2002**, *2*, 87.
[12] R. He, M. Law, R. Fan, F. Kim, P. Yang, *Nano Lett.* **2002**, *2*, 1109.
[13] J. Hu, Y. Bando, Z. Liu, T. Sekiguchi, D. Golberg, J. Zhan, *J. Am. Chem. Soc.* **2003**, *125*, 11 306.
[14] a) T. Yamamoto, *Jpn. J. Appl. Phys., Part 2* **2003**, *42*, L514. b) A. Gokarna, S. V. Bhoraskar, N. R. Pavaskar, S. D. Sathaye, *Phys. Status Solidi A* **2000**, *182*, 175.
[15] a) A. Liu, R. Jones, L. Liao, D. Samara-Rubio, D. Rubin, O. Cohen, R. Nicolaescu, M. Paniccia, *Nature* **2004**, *427*, 615. b) N. Mathur, *Nature* **2002**, *419*, 573.
[16] a) Q. Li, C. Wang, *Appl. Phys. Lett.* **2003**, *83*, 359. b) Y. C. Zhu, Y. Bando, D. F. Xue, D. Golberg, *J. Am. Chem. Soc.* **2003**, *125*, 16 196. c) Y. Jiang, X. M. Meng, J. Liu, Z. R. Hong, C. S. Lee, S. T. Lee, *Adv. Mater.* **2003**, *15*, 1195. d) C. Ma, D. Moore, J. Li, Z. L. Wang, *Adv. Mater.* **2003**, *15*, 228. e) Y. J. Dong, Q. Peng, Y. D. Li, *Inorg. Chem. Commun.* **2004**, *7*, 370.
[17] a) S. T. Lee, Y. F. Zhang, N. Wang, Y. H. Tang, I. Bello, C. S. Lee, *J. Mater. Res.* **1999**, *14*, 4503. b) G. Gundiah, F. L. Deepak, A. Govindaraj, C. N. R. Rao, *Chem. Phys. Lett.* **2003**, *381*, 579. c) Y. Wu, Y. Cui, L. Huynh, C. J. Barrelet, D. C. Bell, C. M. Lieber, *Nano Lett.* **2004**, *4*, 433.
[18] *Handbook of Chemistry and Physics* (Ed: R. C. Weast), CRC Press, Boca Raton, FL **1975**, B-148.

ADVANCED MATERIALS

[19] a) *Binary Alloy Phase Diagrams*, 2nd ed., Vol. 3 (Eds: T. B. Massalski, H. Okamoto, P. R. Subramanian, L. Kacprazak), ASM Int., Materials Park, OH **1990**, p. 3362. b) *Handbook of Ternary Alloy Phase Diagrams*, Vol. 10 (Eds: P. Villars, A. Prince, H. Okamoto), ASM Int., Materials Park, OH **1995**, p. 13 439.
[20] N. H. Tran, A. J. Hartmann, R. Lamb, *J. Phys. Chem. B* **2000**, *104*, 1150.
[21] I. Barin, *Thermochemical Data of Pure Substances*, VCH, Weinheim, Germany **1989**.

Preparation of Functional Nanoporous Silica for Encapsulation of CdSe Nanoparticles**

By *Chang Do Ki*, *Todd Emrick*,* and *Ji Young Chang**

Nanoporous silica materials prepared from surfactant templates contain pore structures that are of interest for catalysis, separations, and molecular imprinting and engineering.[1] Suitable methods for effective pore functionalization will provide considerably more diverse application opportunities than are available at present. Two methods have been reported for the preparation of functionalized mesoporous silica: 1) grafting of a functionalized monolayer in the pores; and 2) co-condensation of functional alkoxysilanes (i.e., $[R'(RO)_3Si]$) with the tetraalkoxysilanes used in the conventional preparation of nanoporous silica.[2] While some recent advances are producing favorable results, considerable challenges remain with regard to the controlled introduction of functionality into the pores. In addition, as only a limited number of functionalized organoalkoxysilanes are commercially available, new synthetic methods designed to tailor the functionality of nanoporous silica will open new opportunities in functional-composite materials science.

Here we report a new methodology for functionalizing nanoporous silica using an amphiphilic organotrialkoxysilane designed to integrate an affinity for nanoparticles into the nanoporous silica structure. The chosen silane contains a thermally labile urethane moiety, which upon heating dissociates to produce an isocyanate functionality tethered to the silica structure.[3] The organotrialkoxysilane used in this work is amphiphilic, and is thus expected to act as a surfactant in the gelation with tetraethoxysilane, forming a micellar structure where the hydrophobic portion is located inside the micelle. The presence of the isocyanate moieties in the nanoporous structure can be exploited in numerous ways; for example, through nucleophilic chemistry for structural and chemical modification. Described below is a method for producing thiol-functionalized nanoporous silica for encapsulation of cadmium selenide nanoparticles (quantum dots). The impressive optical and electronic properties of CdSe nanoparticles make them attractive for integration into nanoporous polymer thin films[4] and silica-based materials, with potential applications in nanoparticle-based devices such as sensors, active displays, light-emitting diodes, etc.[5]

Tetra(ethylene glycol) nonyl ether (TEGNE)-phenol-Si, the key molecule for this study, was prepared as shown in Scheme 1. This amphiphilic molecule consists of a nonyl aliphatic chain, a tetra(ethylene glycol) spacer, and a reactive triethoxysilyl group. In the synthesis, 1-bromononane was first substituted with tetra(ethylene glycol) in tetrahydrofuran (THF) at 75 °C to afford TEGNE. TEGNE was tosylated in dichloromethane, then end-capped with hydroquinone in THF to give a chain-end phenol. Finally, TEGNE-phenol was functionalized with 3-(triethoxysilyl)propyl isocyanate in THF in the presence of dibutyltin dilaurate to give the urethane-linked TEGNE-phenol-Si.

Nanoporous silica (NPS) materials were fabricated by sol–gel chemistry, by co-condensation of a mixture of TEGNE-phenol-Si and tetraethyl orthosilicate (TEOS) as illustrated in Figure 1. TEGNE-phenol-Si (0.075 g) was added to a solution of 1 M HCl (2.5 mL) in methanol (1 mL). The initially turbid reaction mixture became clear upon stirring for 30 min at 50 °C. To this solution TEOS (0.3 g) was added, and the mixture was stirred for 3 h at the same temperature to give a transparent monolithic gel. This was dried under vacuum for three days at room temperature to give a nanoporous material with TEGNE integrated into the structure. Transmission electron microscopy (TEM) showed that the pores had a size distribution narrow enough for many applications, although they did not form a periodic structure (Fig. 1). An average pore diameter of around 10 nm was estimated by TEM.

The thiol groups needed for nanoparticle ligation were introduced into the nanoporous structure by heating TEGNE-functionalized silica to 130 °C in *N*,*N*′-dimethylformamide in the presence of 1,9-nonanedithiol, as depicted in Scheme 2. At this elevated temperature, urethane cleavage generates isocyanate groups at the pore walls, which can then react with 1,9-nonanedithiol.[6] Successful thiol functionalization of the pores was confirmed by solid-state ^{13}C NMR spectroscopy (Fig. 2). In the material obtained after heating in the presence of the thiol, no signals were observed for the TEGNE-phenol, indicating successful cleavage and release from the nanopo-

[*] Prof. T. Emrick
Polymer Science and Engineering Department
University of Massachusetts
120 Governors Drive, Amherst, MA 01003 (USA)
E-mail: tsemrick@mail.pse.umass.edu
Prof. J. Y. Chang, C. D. Ki
School of Materials Science and Engineering
Seoul National University
San 56-1, Shillim-dong, Kwanak-ku, Seoul 151-744 (Korea)
E-mail: jichang@snu.ac.kr

[**] Financial support from the Korea Science and Engineering Foundation through the Hyperstructured Organic Materials Research Center is gratefully acknowledged. T. E. acknowledges the support of a CAREER Award from the National Science Foundation (CHE-0239486), a gift from the Eastman Kodak Company, and facilities support from the NSF-sponsored Materials Research Science and Engineering Center (MRSEC) at UMass Amherst (DMR-0213695).

  DOI: 10.1002/adma.200400184